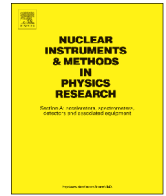




Contents lists available at ScienceDirect

Nuclear Instruments and Methods in Physics Research A

journal homepage: www.elsevier.com/locate/nima

Improved track-etch neutron radiography using CR-39

M.A. Stanojev Pereira^{a,*}, J.G. Marques^a, R. Pugliesi^b, J.P. Santos^a^a C2TN, Instituto Superior Técnico, Universidade de Lisboa, Estrada Nacional 10, km 139.7, 2695-066 Bobadela LRS, Portugal^b Instituto de Pesquisas Energéticas e Nucleares, Centro do Reator de Pesquisas, Av. Prof. Lineu Prestes 2242, Cidade Universitária, 05508-000 São Paulo, Brazil

ARTICLE INFO

Article history:

Received 12 February 2014

Received in revised form

22 July 2014

Accepted 31 July 2014

Available online 7 August 2014

Keywords:

SSNTD

Neutron radiography

Track-etch radiography

ABSTRACT

Currently most state-of-the-art setups for neutron radiography use scintillator screens and CCD cameras for imaging. However, in some situations it is not possible to use a CCD and alternatives must be considered. One such alternative is the well-established technique of track-etch neutron radiography, which has as main disadvantages requiring a long time for image recording and generating images with a relatively low contrast. In this work we address these negative issues and report significant improvements to recording and digitizing images using an improved setup consisting of an enriched ^{10}B converter, a CR-39 solid state nuclear track detector and a flatbed scanner. The improved setup enables a significant reduction of the fluence required to obtain a neutron radiography image using this technique. Comparisons are made with imaging using two CCD models in the same beam line, so that the results can be extrapolated for other facilities.

© 2014 Elsevier B.V. All rights reserved.

1. Introduction

Neutron radiography is an important imaging technique which can be implemented even in research reactors with relatively low flux neutron beams [1]. Image formation and recording was traditionally done using Gd converters in close contact with photographic film [2]. Currently most state-of-the-art setups use scintillator screens coupled to CCD cameras for imaging [3,4]. However, in some situations, e.g., when intense radiation fields are present, it is not possible to use a CCD since these are prone to radiation damage [5,6] and alternatives for image recording must be considered. In this work we have revisited an old technique for image recording based on the use of Solid State Nuclear Track Detectors (SSNTD) [7], to which we introduced several improvements.

SSNTD have been used for charged particle detection for several decades [7]. Their use for thermal neutron radiography requires a suitable converter screen [8] typically using natural boron as a neutron to charged particle converter. The α and ${}^7\text{Li}$ particles released from the nuclear reaction $^{10}\text{B}(n,\alpha){}^7\text{Li}$ induce damages in the molecular structure of the detector, which are visible only by electron microscopes. However, after chemical etching, the damages are enlarged thousands of times, becoming cone-shaped tracks and forming an image which is visible by the

naked eye [9]. An image obtained with a SSNTD exhibits a very low contrast [7] and this has been the main disadvantage of the track-etch neutron radiography technique for practical purposes. Several options to digitize the images obtained with a SSNTD were previously explored [10,11]. In this work we used an enriched boron-10 converter (40 μm thick, Dosirad, France), a CR-39 SSNTD (500 μm thick, Pershore Mouldings, UK) and a low cost flatbed scanner for recording and digitizing images in a low flux neutron beam port of the Portuguese Research Reactor (RPI). Comparisons are made with two CCD models, so that the results can be extrapolated for higher flux facilities.

2. Radiography setup

The RPI is a 1 MW pool-type reactor, supporting a wide range of activities such as neutron activation analysis [12], studies of defects in materials [13,14] and development and calibration of detectors for dark matter search [15]. Most activities are supported through in-pool irradiations with thermal neutron fluxes up to 3×10^{13} n/cm²/s [16]. In order to increase the applications of neutron beam techniques, a setup for neutron imaging was recently installed in the horizontal access of the thermal column of the RPI. The detection system uses a scintillator converter screen and a CCD camera for imaging [17].

Fig. 1 shows a simplified view of the thermal column of the RPI. This irradiation facility is a stacking of graphite with an in-pool pyramidal part and an out-of-pool parallelepipedic part. The

* Corresponding author.

E-mail address: mstanojev@ctn.ist.utl.pt (M.A.S. Pereira).

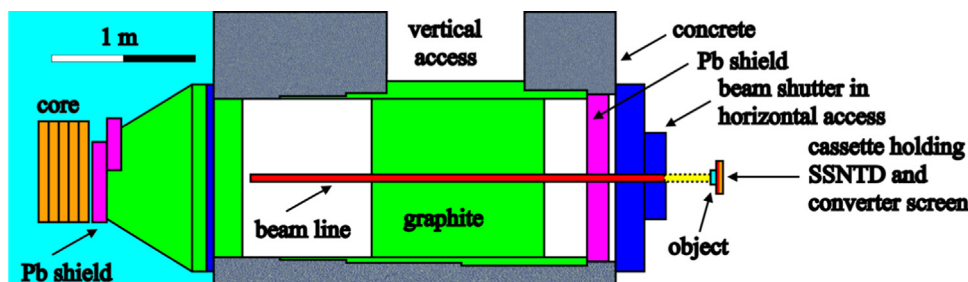


Fig. 1. Simplified view of the horizontal access of the thermal column of the RPI, where the neutron imaging setup is installed. A parallel beam is obtained with an aluminum tube inserted in the graphite moderator. The object to be imaged is shown in front of a film cassette holding a converter and a SSNTD.

parallelepipedic part is enclosed inside an aluminum box embedded in the pool structure. In its original configuration, the horizontal access had about 3 m of graphite until the core edge, resulting in a too low intensity thermal neutron beam. An aluminum tube with inner diameter of 5 cm was inserted in the central part of the graphite moderator, so that the neutrons traveling through this tube are only subjected to the effect of 90 cm of graphite since the core. The thermal neutron flux at the position for radiography is 3×10^5 n/cm²/s. This beam is highly thermalized, with an epithermal flux (at 1 eV) of only 230 n/cm²/s. The simultaneous gamma dose rate was reduced to 12 mGy/h using a Pb filter at the core edge. The beam diameter is $D=5$ cm, with a collimation ratio $L/D=20$. Although the beam intensity and diameter are small, they are enough to image small objects and show the usefulness of the technique [18,19].

The imaging system uses a scintillator screen (0.42 mm thick, Applied Scintillation Technologies, UK) based on ⁶LiF/ZnS, coupled to a Proline 1001E camera (Finger Lakes Instrumentation, USA) equipped with a KAF-1001E CCD [20] (1024 × 1024 pixels) or coupled to an Atik 11000-M camera (Atik Cameras, UK) equipped with a KAI-11002 CCD [21] (4008 × 2672 pixels).

For imaging with a SSNTD, the neutron to charged particle converter used in this work is a 90% ¹⁰B-enriched screen, model BE10 [22], consisting of a 40 μm thick boron layer deposited on a 100 μm polyester substrate. The converter screen and the CR-39 detector are placed in close contact inside a film cassette placed behind the object to be imaged, as shown in Fig. 1. For imaging with a CCD-based setup, the scintillator screen is placed in the same position as the film cassette, inside a light-tight box with a mirror so that the CCD can be mounted perpendicularly to the beam, some 20 cm away [17].

The density of the boron layer in the boron converter is 1.0 g/cm³ [22], significantly less than the density of bulk boron, 2.35 g/cm³ [23]. Table 1 shows the ranges of the particles released from the ¹⁰B(n,α)⁷Li in the converter and in the CR-39 detector, obtained with the SRIM code [24]. The use of converters made of natural boron is more common [9]. However, since natural boron has only 20% of ¹⁰B, the isotope useful for conversion, we have opted to use a converter made with enriched material, in order to get a higher reaction rate and thus a lower exposure time.

The efficiency of the converter is in practice limited by the range of the particles released from the ¹⁰B(n,α)⁷Li reaction [25]. The converter is commonly placed in front of the detector. In this case a thick converter will have a higher overall reaction rate than a thin one, but will also retain a higher amount of the released particles, thus there will be an optimum thickness. However, for foil detectors such as the CR-39 it is also possible to place the converter behind the detector. Fig. 2 shows MCNPX [26] calculations of the amount of released α and ⁷Li particles, as a function of the thickness of the converter, for these two geometries. The Neutron Capture Ion Algorithm of MCNPX was used to follow the fragments from the ¹⁰B(n,α)⁷Li reaction. The cutoff for α and ⁷Li particles was 1 keV.

The amount of released α particles attains a maximum (5.1% per incident neutron) for a converter thickness just below 10 μm,

Table 1

Ranges of the particles released from the ¹⁰B(n,α)⁷Li reaction in the converter screen and in the CR-39 detector calculated with the SRIM code.

Particle	Energy (MeV)	Branching ratio (%)	Range in boron converter (μm)	Range in CR-39 detector (μm)
α	1.47	96.0	8.3	7.1
⁷ Li	0.84	96.0	4.3	3.7
α	1.78	4.0	10.3	8.6
⁷ Li	1.02	4.0	4.9	4.1

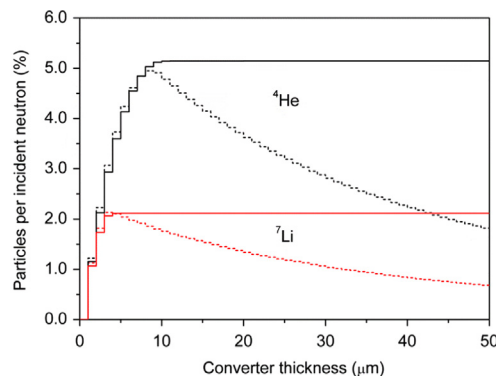


Fig. 2. Simulated amount of α and ⁷Li particles reaching the CR-39 detector, per incident thermal neutron, as function of the thickness of the boron converter, placed behind the detector (continuous lines) and in front of the detector (dashed lines).

while the maximum of ⁷Li particles (2.1% per incident neutron) is attained for a thickness of ~ 4 μm. While the number of particles drops significantly for higher thickness values when the converter is placed before the detector, it remains at its maximum when it is placed after the detector. As the thickness of the converter commercially available is higher than the optimal for thermal neutrons, we have chosen the post-detector configuration.

The α particle energy spectrum is basically the sum of two rectangular distributions, with maximum energy 1.47 MeV (96% relative height) and 1.78 MeV (4% relative height) with a low energy tail. The ⁷Li energy spectrum follows the same trend, with maxima at 0.84 and 1.02 MeV. Fig. 3 shows simulated energy spectra of α and ⁷Li particles released from a 50 μm converter placed post-detector, obtained with the MCNPX code.

The α and ⁷Li particles that reach the CR-39 detector will be stopped within a few micrometers, as can be expected from the data in Table 1. Fig. 4 shows the depth distribution of these particles, in 250 nm intervals.

3. Characterization of the irradiated CR-39 detector

Several sets of “converter screen-detector” were irradiated during periods in the range of 10 s to 8 h, corresponding to a

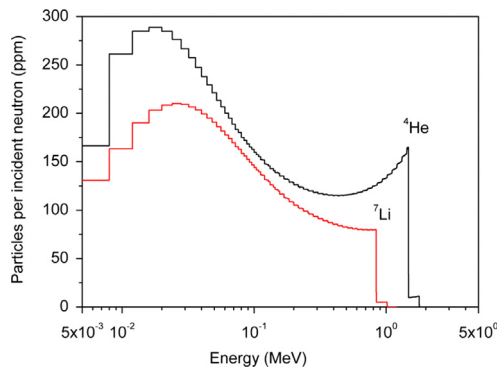


Fig. 3. Simulated energy spectra of α and ${}^7\text{Li}$ particles released from a $50\ \mu\text{m}$ converter, placed post-detector.

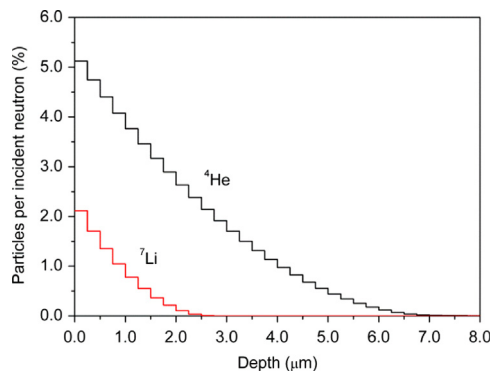


Fig. 4. Simulated depth profile in the CR-39 detector of α and ${}^7\text{Li}$ particles released from a $50\ \mu\text{m}$ converter, placed post-detector.

thermal neutron fluence in the range 3.0×10^6 – $8.6 \times 10^9\ \text{n/cm}^2$ and an α particle fluence in the range 1.5×10^5 – $4.4 \times 10^8\ \alpha/\text{cm}^2$. After irradiation and etching, the initially transparent CR-39 gets a mild translucent aspect, which is clearly visible with the naked eye.

Chemical etching of the CR-39 was performed in a standard aqueous solution (30% KOH) at $70\ ^\circ\text{C}$, during 25 min. These conditions were previously optimized [9,27]. Etching in these conditions removes $0.049 \pm 0.002\ \mu\text{m}/\text{min}$, i.e., about $1.2\ \mu\text{m}$. From the data in Fig. 4, the slice removed by chemical etching corresponds to a region where 50% of the α particles were stopped and 91% of the ${}^7\text{Li}$ were stopped. Thus the images to be analyzed were created mostly by the damage due to the α particles from the ${}^{10}\text{B}(n,\alpha){}^7\text{Li}$ reaction. After etching, the detectors were washed in a water stream and dried by using a soft absorbent paper.

UV–visible spectroscopy of the CR-39 detectors after etching was done using a Shimadzu UV-1800 spectrophotometer. The scanning speed of the apparatus was $1200\ \text{nm}/\text{min}$ and the scanning wavelength region was 200 – $800\ \text{nm}$. Fig. 5 shows the variation with wavelength of the absorbance (logarithmic ratio of the radiation falling upon the CR-39, to the radiation transmitted through it) of the irradiated detectors, together with the corresponding variation for a virgin sample and a CR-39 irradiated for 8 h with neutrons only (i.e., without converter), for comparison. The wavelength of the absorption edge shifts towards higher values with the increase of irradiation time, in the range 250 – $300\ \text{nm}$. For irradiations up to 2 h the spectrum is essentially flat in the visible region; for longer irradiations there is a marked decrease in the absorbance above $600\ \text{nm}$. The spectrum of the CR-39 irradiated only with neutrons is the closest to the virgin one, confirming that the above mentioned effects are mostly due to the charged particles released from the ${}^{10}\text{B}(n,\alpha){}^7\text{Li}$ reaction. Fig. 6 shows the absorbance at $530\ \text{nm}$ as function of the

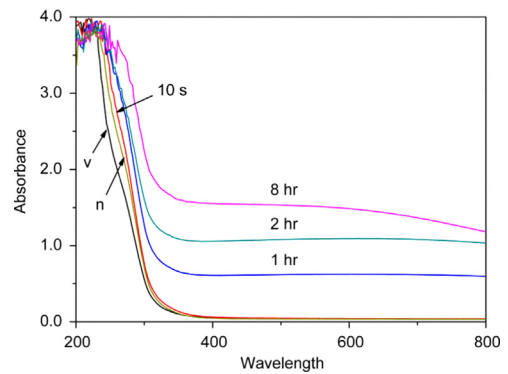


Fig. 5. UV–visible spectra of the irradiated CR-39 as a function of the irradiation time, compared with a virgin (v) sample and one irradiated for 8 h with neutrons only (n).

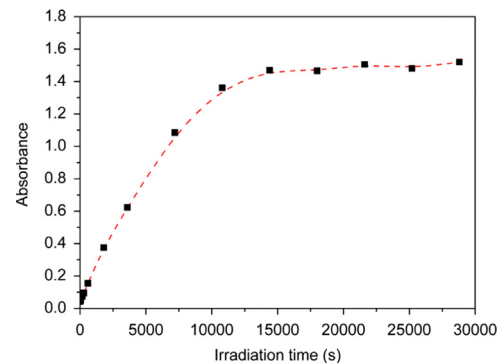


Fig. 6. Variation of the absorbance at $530\ \text{nm}$ as function of the irradiation time. The dashed line was drawn to guide the eye only.

irradiation time. The variation is approximately linear for irradiations up to about 2 h. The same behavior is generally seen for all wavelengths in the visible region.

4. CR-39 image digitalization

4.1. Scanning of images

Flatbed scanners are increasingly used as a low cost tool to digitize images in several applications [28–31]. In this work we have used 4 different commercial flatbed scanners, with properties indicated in Table 2. These scanners use 3 different types of light sources: cold cathode fluorescent lamp, red–green–blue LEDs and white LED. Although the spectra from these light sources are different [32], this should have no impact given the essentially flat curves in the visible region shown in Fig. 5.

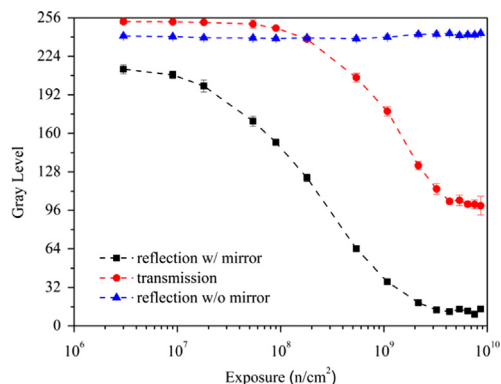
Scans were made in reflection mode and in transmission mode when the scanner also had a second light source placed in the lid. Reflection was enhanced with the use of a thin mirror placed in the back of the CR-39. The VueScan 9 code [33] was used to control all scanners and obtain images in 8 or 16 bits grayscales, with all filters and compensations switched off. The resolution was $2400\ \text{dpi}$ in all cases, with each dot corresponding to a nominal area of $11\ \mu\text{m} \times 11\ \mu\text{m}$.

Fig. 7 shows typical gray level (GL) readings (8 bits scale) of the irradiated CR-39 detectors obtained using an Epson V500 flatbed scanner in transmission and reflection modes as function of neutron exposure (E). The GL corresponding to each exposure was evaluated by averaging the intensity of about 1500 individual pixels. In the “normal” reflection mode the irradiated CR-39 detectors are hardly distinguishable, showing essentially the same

Table 2

General properties of the flatbed scanners used in this work.

Manufacturer	Model	Light source ^a	Optical sensor	Mode ^b
Canon	3200f	CCFL	CCD	r
Canon	LIDE 110	RGB LEDs	CIS	r
Epson	V500	White LED	CCD	t/r
HP	4370	CCFL	CCD	t/r

^a CCFL—cold cathode fluorescent lamp.^b r—Reflection; t—transmission.**Fig. 7.** Gray level readings (8 bits) of the irradiated CR-39 detectors on an Epson V500 flatbed scanner in transmission and reflection modes. The lines were drawn to guide the eye.**Table 3**

Dynamic range (DR) in reflection (enhanced with mirror) and transmission modes using 8 and 16 bits gray scales.

Manufacturer	Model	DR reflection (8 bits)	DR reflection (16 bits)	DR transmission (8 bits)	DR transmission (16 bits)
Canon	3200f	6.4	3.3	–	–
Canon	LIDE 110	4.7	2.0	–	–
Epson	V500	4.6	3.2	2.1	2.1
HP	4370	5.1	3.0	–	–

white levels. In contrast, in transmission mode they are well separated until irradiation times of approximately 10,000 s (corresponding to an exposure of 3×10^9 n/cm²), in agreement with the trend shown in Fig. 5 for the absorbance at 530 nm. However, we found that a better dynamic range is obtained in reflection mode enhanced with a mirror behind the CR-39. The dynamic range was determined from the ratio between the largest and smallest value of gray level obtained in steepest part of the curve of GL vs. E. The corresponding curves obtained with the other scanners follow the same general trends. Table 3 presents the results obtained with the four scanners.

The following operational parameters of the technique were determined: exposure interval for best contrast, spatial resolution, and sensitivity.

4.2. Exposure interval for best contrast

The exposure interval for best contrast in the image was determined from the curve GL vs. E. The contrast is defined by $G = \Delta GL / \Delta(\log E)$ and attains its maximum in the steeper region of this curve [15]. Fig. 8 shows the curves obtained with the 4 flatbed image scanners, using an 8 bits gray scale, for the irradiated SSNTDs after etching where again the GL corresponding to each

exposure was evaluated by averaging the intensity of about 1500 individual pixels. The general form of the curves is the same and the best contrast was achieved in the exposure range 5.4×10^7 – 1.1×10^9 n/cm². Thus the optimum irradiation time was taken as 1 h, corresponding to an exposure of 1.1×10^9 n/cm².

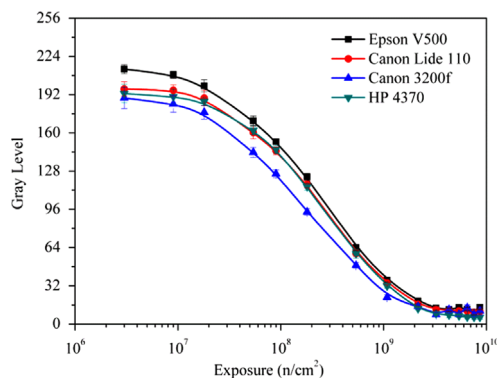
The differences due to digitizing of the images are relatively small. Table 4 shows the values for the contrast G obtained with the 4 flatbed image scanners, using 8 and 16 bits gray scales. The G values obtained using a 16 bits gray scale were divided by 256 for a direct comparison with the G values obtained using an 8 bits scale. Table 4 shows that scanner model Epson V500 is marginally better. All scanners show a similar performance using 8 and 16 bits gray scales, except model Canon 3200f, which shows a worse performance at 8 bits. One should mention that the scanners are here being used in a task for which they are not necessarily optimized. When scanning a Kodak gray scale (Ref. 1527654) the performance of the four scanners is virtually identical.

The values obtained here compare favorably with previous results. The optimum fluence for CR-39 when using a natural boron screen has been determined to be 7.7×10^9 n/cm², while the obtained mean contrast was 90 ± 6 [10]. Thus an exposure reduction by a factor of 7 has been obtained in this work. From the ratio of the enrichment of the screens (90% vs. 20%) one would expect a gain by a factor of ~ 4.5 . The extra gain and the larger contrast are due to the improved scanning of the images.

HP 4370 scanner was chosen for the characterization of spatial resolution and sensitivity, as effects of automatic compensation were still visible when using the other scanners, even if this option was disabled in the VueScan software.

4.3. Spatial resolution

The spatial resolution is defined as the smallest distance that can be distinguished between two objects [34]. Usually it is given in terms of total resolution (U_t), which is the sum of the intrinsic

**Fig. 8.** Variation of the gray level as a function of the neutron exposure obtained with 4 flatbed image scanners using an 8 bits scale. The lines were drawn to guide the eye.**Table 4**

Values for the image contrast obtained with four flatbed image scanners using 8 and 16 bits gray scales.

Scanner	8 bit	16 bit ^a
Epson V500	107 ± 2	107 ± 2
Canon Lide 110	102 ± 3	102 ± 3
Canon 3200f	94 ± 3	101 ± 2
Hewlett-Packard 4370	104 ± 3	104 ± 2

^a Divided by 256 to allow direct comparison.

resolution (U_i) from the imaging system, and the geometric resolution (U_g), from the angular divergence of the neutron beam, expressed by Eq. (1) [35].

$$(U_t)^n = (U_i)^n + (U_g)^n, \quad 1 < n < 3 \quad (1)$$

A neutron opaque plate (Gd knife-edge foil, 127 μm thick) was the standard object used for self evaluation. It was irradiated for 1 h in a tight contact to the detector-converter set. For this condition $U_g \sim 0$, and $U_t \sim U_i$, and according to Eq. (1) the value for U_t corresponds to the best resolution achievable. After etching and digitizing, the GL distribution at the edge of the image registered in the detector was scanned. The Edge Spread Function (ESF) [32], Eq. (2), is fitted to the distribution and U_t is given by Eq. (3) [10,32].

$$\text{ESF} = p_1 + p_2 a \tan [p_3(x - p_4)] \quad (2)$$

$$U_t = 2/p_3 \quad (3)$$

In Eq. (2), p_1 , p_2 , p_3 and p_4 are free parameters and x is the scanning coordinate. Fig. 9 shows one of the obtained fits. The resolution was evaluated as an average of five measurements performed at different locations of the image and the result was $U_t = 62 \pm 4 \mu\text{m}$. The contribution to this value of the scanner at 2400 dpi can be neglected.

4.4. Sensitivity

Sensitivity is the capability of the technique to discern thickness variations of a material. It was evaluated by means of curves that relate the GL in the image as a function of the sample thickness. The samples are step wedges manufactured in polyethylene, copper and iron, with thickness varying from 2.5 to 12.5 mm in 6 steps, which were irradiated for about 1 h. After etching and image digitizing, the values of gray levels as functions of the thickness were determined. The result is shown in Fig. 10, where the linear function Eq. (4) [9] was fitted to the obtained data.

$$\text{GL}(x) = \text{GL}_0 - Cx \quad (4)$$

In Eq. (4), GL_0 is the gray level intensity for the direct beam. The sensitivity Δx corresponding to a ΔGL variation, and is expressed by Eq. (5) [9,32].

$$\Delta x = \Delta \text{GL}/C \quad (5)$$

By taking into account the values for the parameter C , and for a $\Delta \text{GL} = 5$, the sensitivity for polyethylene, iron and copper are $0.53 \pm 0.02 \text{ mm}$, $0.87 \pm 0.01 \text{ mm}$ and $0.96 \pm 0.03 \text{ mm}$, respectively.

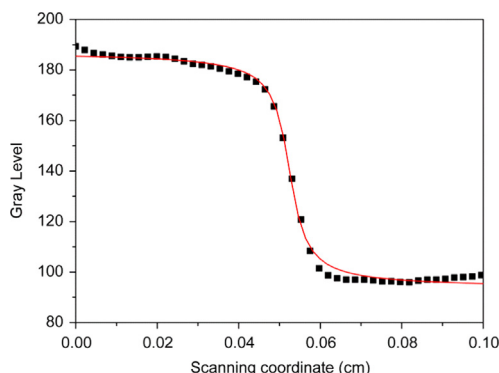


Fig. 9. Distribution of the gray level intensity as a function of the scanning coordinate.

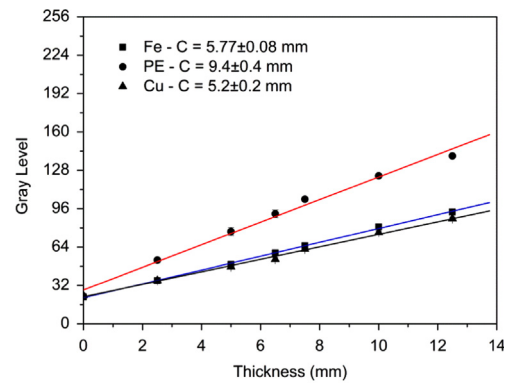


Fig. 10. Variation of the gray level as a function of sample thickness.

Table 5

Resolution, pixel size, image size, peak quantum efficiency (QE), QE at 530 nm and charge transfer efficiency for the KAF-1001 and KAI-11002 CCD models used in the Proline 1001E and Atik 11000-M cameras, respectively [19,20].

Parameter	KAF-1001	KAI-11002
Resolution	1024 (H) × 1024 (V)	4008 (H) × 2672 (V)
Pixel size [μm]	24 (H) × 24 (V)	9.0 (H) × 9.0 (V)
Image size [mm]	24.6 (H) × 24.6 (V)	36.0 (H) × 24.0 (V)
Peak QE	0.73	0.51
QE at 530 nm	0.53	0.47
CTE	> 0.99997	> 0.99999

5. Comparison with CCD imaging

Currently most state-of-the-art setups use scintillator screens coupled to CCD cameras for imaging. There is a huge variety of CCD cameras developed for the industry and astronomy markets, amongst others. The performance of a CCD depends on its ability to generate, collect, transfer and measure charge [6]. Unfortunately, not all relevant parameters are specified by the different manufacturers in a clear way that permits a direct comparison between CCD models.

Table 5 shows the values for resolution, pixel size, image size, Quantum Efficiency (QE) and Charge Transfer Efficiency (CTE) for the KAF-1001 and KAI-11002 CCD models used in the Proline 1001E and Atik 11000-M cameras, respectively, available at our facility. QE quantifies charge generation and is defined as the fraction of incident photons that produce a useful charge, while CTE quantifies charge transfer which is accomplished by manipulating the voltage on a parallel sequence of gates that form a CCD register. While the QE is marginally better for the KAF-1001, the CTE is significantly better in the more recent KAI-11002 CCD. Fig. 11 shows the variation with wavelength of the QE for the two CCD models, together with the spectral response of the $^6\text{LiF/ZnS}$ scintillator, with a peak at 530 nm.

Fig. 12 shows the variation of the gray level as a function of neutron exposure in the range $1 \times 10^5 < E < 6 \times 10^8 \text{ n/cm}^2$, for the Atik camera at -15°C using 2×2 binning, thus with an effective pixel size of $18 \mu\text{m} \times 18 \mu\text{m}$. A total of 11 points have been obtained, and each one is evaluated by averaging the gray-level intensities of about 1500 individual pixels in the image. According to the curve, the best dynamic range corresponds to a maximum exposure of $2 \times 10^7 \text{ n/cm}^2$ or 1.1 min of irradiation. This exposure is 4.5 times lower than the one previously obtained with the Proline 1001E camera [15] and 50 times lower than the one obtained in this work with the CR-39 detector. The spatial resolution obtained was $285 \pm 28 \mu\text{m}$, slightly better than obtained before with the Proline 1001E camera, $391 \pm 10 \mu\text{m}$ [15].

6. Application examples

In order to demonstrate the potential of the implemented technique, some objects were radiographed using the SSNTD-based setup and the CCD-based (Atik camera) setup at the RPI.

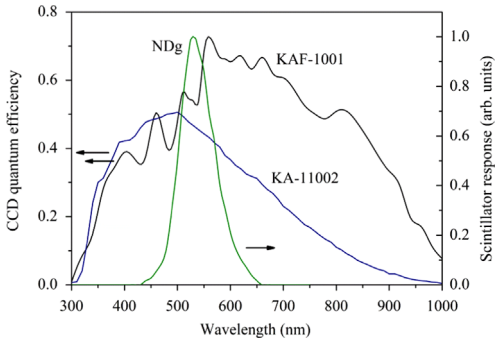


Fig. 11. Quantum efficiency of the KAF-1001 and KA-11002 CCD as function of wavelength and spectral response of the ⁶LiF/ZnS scintillator.

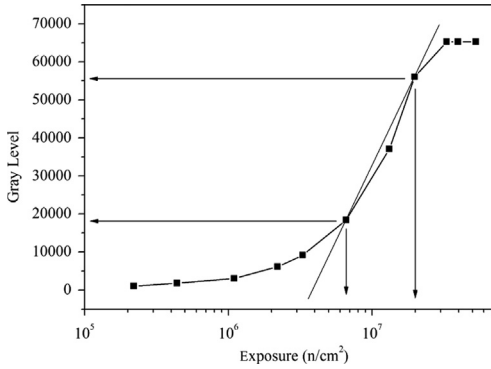


Fig. 12. Gray level obtained with the Atik 11000 camera as function of the neutron exposure. The best dynamic range is obtained with an exposure of 2 × 10⁷ n/cm².

Fig. 13 shows the images obtained for an ordinary gas lighter, consisting of an external plastic body and several metallic parts. The level of the flammable gas inside the plastic body is clearly visible, as are the metallic roller and cap on top. Fig. 14 shows the radiography of the top of an insecticide spray can containing several plastic components inside a metallic body. The presence of insecticide inside the tubing is clearly visible.

Figs. 13 and 14 show that the images obtained with the two imaging methods display a comparable detail. The differences on the images are mostly a result of the different spatial resolutions achieved in the beam line of the RPI, which favors the SSNTD-based setup, as discussed in the previous sections.

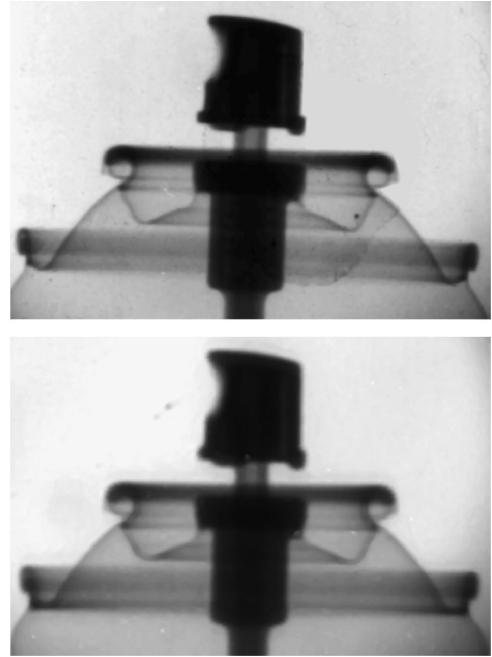


Fig. 14. Radiographies of the top of an insecticide spray can obtained with a SSNTD-based setup (top) and a CCD-based setup (down).

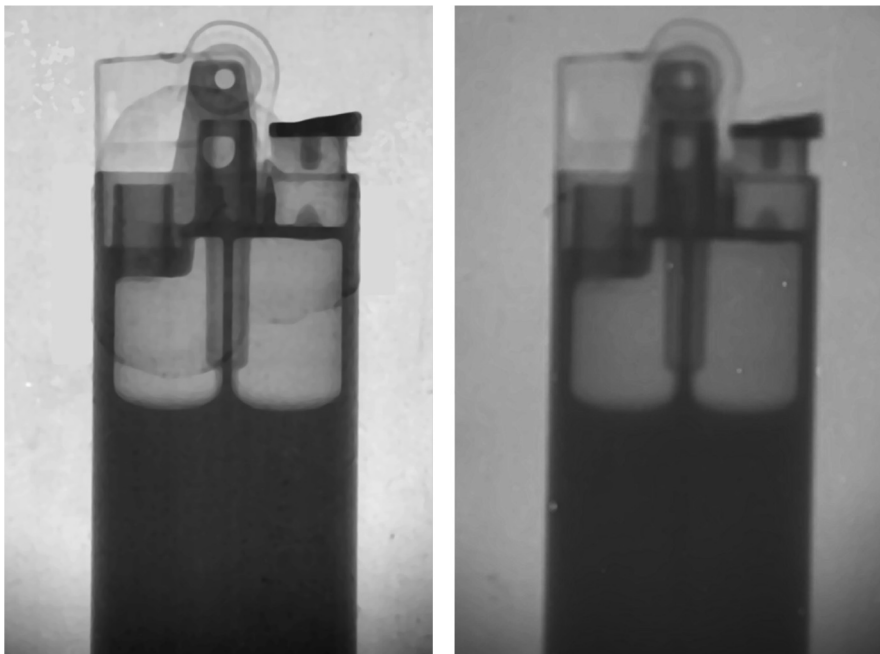


Fig. 13. Radiographies of an ordinary gas lighter obtained with a SSNTD-based setup (left) and a CCD-based setup (right).

7. Conclusions

We have revisited an old technique for neutron radiography imaging and introduced several improvements. Based on the obtained images and results, it is clear that the SSNTD CR-39 associated with a boron-enriched screen and a light transmission scanner for image digitizing exhibits good characteristics for neutron radiography purposes. The best image in terms of contrast and resolution was achieved for a neutron exposure of 1.1×10^9 n/cm², corresponding to an irradiation time of about 1 h in a low flux beam port of the RPI and an etching time of 25 min. Image digitizing can be done with simple flatbed scanners, common for home and office use. A reduction factor of 7 in exposure has been achieved when comparing with previous results using a natural boron converter. This reduction results from the increased enrichment of the boron converter and better procedures for digitizing the images.

By comparing the operational characteristics of the track-etch technique with the ones for the scintillator plus a CCD camera system, installed in the same facility, the main differences between them are the longer time required for image acquisition (10–50 times, depending on the characteristics of the CCD) and the need of chemical etching. On the other hand, the intrinsic resolution in our setup with a parallel beam is 300–400 μm for the CCD-based setup while it is only 62 μm for the SSNTD-based setup. Despite its longer exposure time, the CR-39 is a viable alternative for neutron imaging in the presence of intense radiation fields which would damage a CCD. On the other hand, since the cost of the SSNTD method is a fraction of the cost of a system using a CCD camera, this method may also be considered as starting alternative in small facilities where there is no pressure on beam time.

Acknowledgments

This work was partially supported by the FCT, Portugal, under Grant PTDC/HIS-HEC/101756. The installation for neutron tomography at the RPI was funded by FCT, Portugal, under Grant POCI/FIS/59287. Dr. Sandra Cabo Verde is kindly acknowledged for having made available the spectrophotometer used in this work.

References

- [1] International Atomic Energy Agency, Utilization Related Design Features of Research Reactors: A Compendium, Technical Reports Series No. 455, IAEA, Vienna, 2007.

- [2] J.C. Domanus, Practical Neutron Radiography, Kluwer Academic Publishers, Dordrecht, 1992.
- [3] T. Bücherl, Ch. Lierse von Gostomski, H. Breitreutz, M. Jungwirth, F.M. Wagner, Nuclear Instruments and Methods in Physics Research A 651 (2011) 86.
- [4] F.C. de Beer, F. Gruenauer, J.M. Radebe, T. Modise, B. Schillinger, Physics Procedia 43 (2013) 34.
- [5] J.E. Brau, N. Sinev, IEEE Transactions on Nuclear Science NS47 (2000) 1898.
- [6] J.R. Janesick, Scientific Charged-Coupled Devices, Bellingham, SPIE Press, 2001.
- [7] H. Berger, Nuclear Technology 19 (1973) 188.
- [8] R. Pugliesi, M.A.P.V. De Moraes, I.M. Yamazaki, Applied Radiation and Isotopes 41 (1990) 601.
- [9] D. Nikezic, K.N. Yu, Materials Science and Engineering R46 (2004) 51.
- [10] M.A. Stanojev Pereira (Ph.D. thesis), University of São Paulo, 2009 (unpublished).
- [11] R. Pugliesi, F. Pugliesi, M.A. Stanojev Pereira, Brazilian Journal of Physics 41 (2011) 123.
- [12] H.M. Dung, M.C. Freitas, J.P. Santos, J.G. Marques, Nuclear Instruments and Methods A 622 (2010) 438.
- [13] J.G. Marques, A. Kling, J.C. Soares, L. Rebouta, M.F. da Silva, E. Diéguez, F. Agulló-López, Nuclear Instruments and Methods B 136–138 (1998) 431.
- [14] J.G. Marques, K. Lorenz, N. Franco, E. Alves, Nuclear Instruments and Methods B 249 (2006) 358.
- [15] F. Giuliani, C. Oliveira, J.I. Collar, T.A. Girard, T. Morlat, D. Limagne, J.G. Marques, A.R. Ramos, G. Waysand, Nuclear Instruments and Methods A 526 (2004) 348.
- [16] A.C. Fernandes, J.P. Santos, J.G. Marques, A. Kling, A. Ramos, N.P. Barradas, Annals of Nuclear Energy 37 (2010) 1139.
- [17] M.A. Stanojev Pereira, J.G. Marques, R. Pugliesi, Brazilian Journal of Physics 42 (2012) 360.
- [18] M.I. Prudêncio, M.A.S. Pereira, J.G. Marques, M.I. Dias, L. Esteves, C.I. Burbidge, M.J. Trindade, M.B. Albuquerque, Journal of Archaeological Science 39 (2012) 964.
- [19] T.P. Silva, M.O. Figueiredo, M.I. Prudêncio, Applied Clay Science 82 (2013) 101.
- [20] Truesense Imaging Inc., KAF-1001 Image Sensor, Revision 1.0 PS-0012, 2012.
- [21] Truesense Imaging Inc., KAI-11002 Image Sensor, Revision 1.0 PS-0033, 2012.
- [22] Dosirad Company, (<http://dosirad.pagespro-orange.fr/>).
- [23] W.M. Haynes (Ed.), CRC Handbook of Chemistry and Physics, 92nd edition, CRC Press, Boca Raton, 2011.
- [24] J.F. Ziegler, J.P. Biersack, U. Littmark, The Stopping and Range of Ions in Solids, Pergamon Press, New York, 1985.
- [25] Z. Wang, C.L. Morris, Nuclear Instruments and Methods A 652 (2011) 323.
- [26] D.B. Pelowitz, MCNPX User's Manual Version 2.7, LA-CP-11-00438, Los Alamos, 2011.
- [27] R. Pugliesi, M.A. Stanojev Pereira, M.A.P.V. de Moraes, M.O. de Menezes, Applied Radiation and Isotopes 50 (1999) 375.
- [28] B.C. Ferreira, M.C. Lopes, M. Capela, Physics in Medicine and Biology 54 (2009) 1073.
- [29] M. Vidal, J.M. Amigo, R. Bro, M. Ostra, C. Ubide, J. Zuriarrain, Analytica Chimica Acta 694 (2011) 38.
- [30] B. Secerov, M. Dakovic, N. Borojevic, G. Bacic, Nuclear Instruments and Methods A 633 (2011) 66.
- [31] H. Alnawaf, P.K.N. Yu, M. Butson, Journal of Applied Clinical Medical Physics 13 (2012) 314.
- [32] C. Cui, in: P.D. Burns, S. Triantaphillidou (Eds.), Proceedings of the SPIE Image Quality and System Performance X Conference, vol. 8653, Burlingame (CA), 2013, p. 86530G.
- [33] (<http://www.hamrick.com>).
- [34] R. Ilic, M. Najzer, Nuclear Tracks and Radiation Measurements 17 (1990) 475.
- [35] P. Von Der Hardt, H. Roettger, Neutron Radiography Handbook: Nuclear Science and Technology, D. Reidl Pub. Co., Dordrecht, 1981.